

Efficient Perovskite Light-Emitting Diodes Using Polycrystalline Core–Shell-Mimicked Nanograins

Min-Ho Park, Jaehyeok Park, Jaeho Lee, Hyeon Seob So, Hobeom Kim, Su-Hun Jeong, Tae-Hee Han, Christoph Wolf, Hosun Lee, Seunghyup Yoo, and Tae-Woo Lee*

Making small nanograins in polycrystalline organic–inorganic halide perovskite (OIHP) films is critical to improving the luminescent efficiency in perovskite light-emitting diodes (PeLEDs). 3D polycrystalline OIHPs have fundamental limitations related to exciton binding energy and exciton diffusion length. At the same time, passivating the defects at the grain boundaries is also critical when the grain size becomes smaller. Molecular additives can be incorporated to shield the nanograins to suppress defects at grain boundaries; however, unevenly distributed molecular additives can cause imbalanced charge distribution and inefficient local defect passivation in polycrystalline OIHP films. Here, a kinetically controlled polycrystalline organic-shielded nanograin (OSN) film with a uniformly distributed organic semiconducting additive (2,2',2''-(1,3,5-benzinetriyl)-tris(1-phenyl-1-*H*-benzimidazole), TPBI) is developed mimicking core–shell nanoparticles. The OSN film causes improved photophysical and electroluminescent properties with improved light out-coupling by possessing a low refractive index. Finally, highly improved electroluminescent efficiencies of 21.81% ph el^{-1} and 87.35 cd A^{-1} are achieved with a half-sphere lens and four-time increased half-lifetime in polycrystalline PeLEDs. This strategy to make homogeneous, defect-healed polycrystalline core–shell-mimicked nanograin film with better optical out-coupling will provide a simple and efficient way to make highly efficient perovskite polycrystal films and their optoelectronics devices.

OIHPs have been followed.^[1–8] The performance of OIHP LEDs (PeLEDs) has been dramatically improved by the interface modification to increase charge injection efficiency and surface morphology,^[9,10] the solvent treatment to control a crystallization and grain size,^[3,11] the use of various additives for a defect passivation,^[12–14] and incorporation of outcoupling structures.^[15–17] In order to achieve highly efficient polycrystalline PeLEDs, making small nanograins in polycrystalline OIHPs is one of the effective ways to improve radiative recombination by spatially confining the excitons or charge carriers inside the grains, because long exciton diffusion length and small exciton binding energy causing high free carrier density in OIHPs limit the radiative recombination rate.^[3,13,14,18] At the same time, passivating the defects at the grain boundaries is also much more critical when the grain size becomes smaller. Colloidal perovskite nanocrystals smaller than a few tens of nanometers are ideal for high-efficiency emitters but they have to include insulating ligand which impedes charge transport in PeLEDs.^[19,20] There-

fore, polycrystalline core–shell-mimicked nanograin shielded by organic semiconductor can be a good approach, which facilitates the charge carrier confinement and charge transport synergistically in PeLEDs.

Additive engineering is a very effective way to reduce a defect density and modify the characteristics of polycrystalline OIHP film. Most of work has been done with liquid or insulating additives.^[21,22] Furthermore, the scientific investigations in terms of

1. Introduction

Organic–inorganic halide perovskites (OIHPs) are the promising emitters that satisfy the requirements including low-cost materials, high color purity, easy color tunability, easy synthesis, and a simple fabrication process. The 3D OIHP polycrystals have been first considered as a simple approach for light-emitting diode (LED) application, while other low-dimensional

Dr. M.-H. Park, Dr. H. Kim, Dr. S.-H. Jeong, Dr. T.-H. Han, Dr. C. Wolf, Prof. T.-W. Lee
Department of Materials Science and Engineering
Research Institute of Advanced Materials
Institute of Engineering Research
Nano System Institute (NSI)
Seoul National University
1 Gwanak-ro, Gwanak-gu, Seoul 08826, South Korea
E-mail: twlees@snu.ac.kr, taewlees@gmail.com

J. Park, Dr. J. Lee, Prof. S. Yoo
School of Electrical Engineering
Korea Advanced Institute of Science and Technology (KAIST)
Daejeon 305-701, South Korea
H. S. So, Prof. H. Lee
Department of Applied Physics
Kyung Hee University
Yong-In 446-701, South Korea

 The ORCID identification number(s) for the author(s) of this article can be found under <https://doi.org/10.1002/adfm.201902017>.

DOI: 10.1002/adfm.201902017

the influence on the crystallization kinetics and the limitation have been rarely considered. Because the “impurity effect” of molecular additives impedes the formation of small grains by increasing the supersaturation and Gibbs energy for nucleation during a conventional film-forming process, the large grain, which is unfavorable for the LED application, is dominantly formed.^[23–25]

Additionally, the charge carrier dynamics and the charge recombination behavior including the formation of a recombination zone in the OIHP emitting layer (EML) are the other important factors to be considered for the efficient PeLEDs.

To control these physical parameters in the devices including grain size, core–shell-like nanograin morphology, charge transport, and charge recombination simultaneously, organic semiconducting materials can be effective additives. When the additives are unevenly distributed throughout the OIHP film, unbalanced electron–hole recombination, local charge accumulation, and uneven photophysical properties can be induced. Therefore, the key challenges to achieve highly efficient polycrystalline PeLEDs are i) the formation of core–shell nanograins shielded with uniform organic molecular additive distribution mimicking core–shell nanoparticle by overcoming the issues related to the large grain formation caused by molecular additives, ii) the effective electron–hole balance and charge distribution, which is accompanied by the modification of the recombination zone position, and iii) a low optical loss by reducing an internal reflection of waveguide mode.^[26]

2. Results and Discussion

Here, we developed kinetically controlled polycrystalline OIHP core–shell-mimicked nanograins shielded with organic semiconducting molecules mimicking core–shell nanoparticles for efficient and stable PeLEDs. To realize this, we devised a new concept called an “organic-shielded nanograins (OSN)” in order to make the uniform distribution of an organic semiconductor additive as a shell throughout the film by preventing the crystal coarsening due to the additive (i.e., impurity). 2,2',2''-(1,3,5-benzinetriyl)-tris(1-phenyl-1-*H*-benzimidazole) (TPBI) and green-emitting CH₃NH₃PbBr₃ (MAPbBr₃) were used as an additive and OIHP nanograins to deposit OSN film, respectively. The control of the additive-based crystal pinning (A-NCP) process induced instantaneous nucleation and a rapid crystal growth by drastically changing the solubility state of the spinning OIHP quasi-film.^[3,14] In other words, the OIHP crystal growth can be instantaneously frozen, so small nanograin cores form, and molecular semiconducting additives are instantaneously confined at the grain boundary region to shield the nanograin cores. Therefore, the OSN film has a homogeneous additive distribution throughout the film, and thus additives effectively filled and healed all defective grain boundaries in the film, which act as nonradiative recombination centers.^[3,14,21,27] Moreover, uniformly distributed TPBI additive throughout polycrystalline MAPbBr₃ film can effectively cause a formation of the broad recombination zone. As a result, MAPbBr₃:TPBI (OSN) PeLED showed high radiative recombination, high electroluminescent (EL) efficiencies, current efficiency (CE) = 87.35 cd A⁻¹, and external quantum

efficiency (EQE) = 21.81% ph el⁻¹, with a half-sphere lens (HS) and four-times increased half-lifetime.

To identify the influence of the organic small molecule additive in OIHP film formation on self-organized conducting polymer (SOCP) anode, we observed the crystal growth behaviors by precisely controlling the TPBI additive concentration ([TPBI]). The MAPbBr₃ precursor solutions, which were prepared by mixing MABr and PbBr₂ precursors and dimethyl sulfoxide (DMSO) as solvent, were mixed with various concentrations of TPBI additives dissolved in chlorobenzene (CB) solvent, and pure MAPbBr₃ and MAPbBr₃:TPBI films were deposited onto the SOCP layer by using the normal one-step spin-coating process. The organic molecular additives dissolved in the OIHP solution with a high concentration severely retard the original OIHP crystallization behaviors, so large crystals can form.^[28–30] This phenomenon is called an “impurity effect” of the additive.^[28] In previous research on perovskite solar cells that incorporated additives in an OIHP layer, the larger grain formation has been observed. The large grains have high carrier mobility due to low charge trap densities, so the larger grains are clearly beneficial in solar cell application.^[29,31,32] However, these large grains cause thermal ionization of electron–hole pairs and thus do not produce high photoluminescence (PL) and EL efficiencies in OIHP layers and their devices. Therefore, it is important to overcome the impurity (i.e., additive) effect to reduce the grain size for the effective exciton confinement inside nanograins to yield high luminous efficiency.^[3] To understand the impurity effect of TPBI as organic small molecular additive in MAPbBr₃ crystallization kinetics, we investigated scanning electron microscope (SEM), X-ray diffraction (XRD), and energy-dispersive spectrometer (EDS) (Figures S1–S7, Supporting Information). Moreover, we investigated in situ Fourier transform infrared (FTIR) transmittance spectra depending on the drying time to study the chemical interaction such as Lewis adduct formation between TPBI additive and perovskite precursors (Figures S8–S10, Supporting Information). From the investigations of real-time FTIR measurement, we confirmed that TPBI additive does not chemically react with perovskite precursors in the presence of relatively stronger Lewis bases of DMSO or dimethylformamide (DMF). Therefore, we concluded that the large grain formation with TPBI additive is mainly caused by the impurity effect, which is accompanied with increasing the supersaturation and Gibbs free energy and Ostwald ripening, and probably caused by the retarded solvent evaporation.

To overcome the impurity effect of TPBI additives and form the core–shell nanoparticle–mimicked small MAPbBr₃ nanograins shielded with uniform TPBI additives, we have approached from the perspective of thermodynamic modification by devising the OSN film process that controls the crystallization kinetics through the drastic solubility change in MAPbBr₃:TPBI quasi-film by using the fast A-NCP process. To deposit the OSN film, 80 μL of TPBI:chloroform (CF) solution was dropped onto the spinning MAPbBr₃:TPBI quasi-film surface with a high dropping speed of 120 μL s⁻¹ (OSN film formation; **Figure 1a**). We described the film formation mechanism during the spin-coating process by using a simplified schematic phase diagram (**Figure S7a**, Supporting Information). The controlled A-NCP process induces a drastic solubility change of OIHP quasi-film from

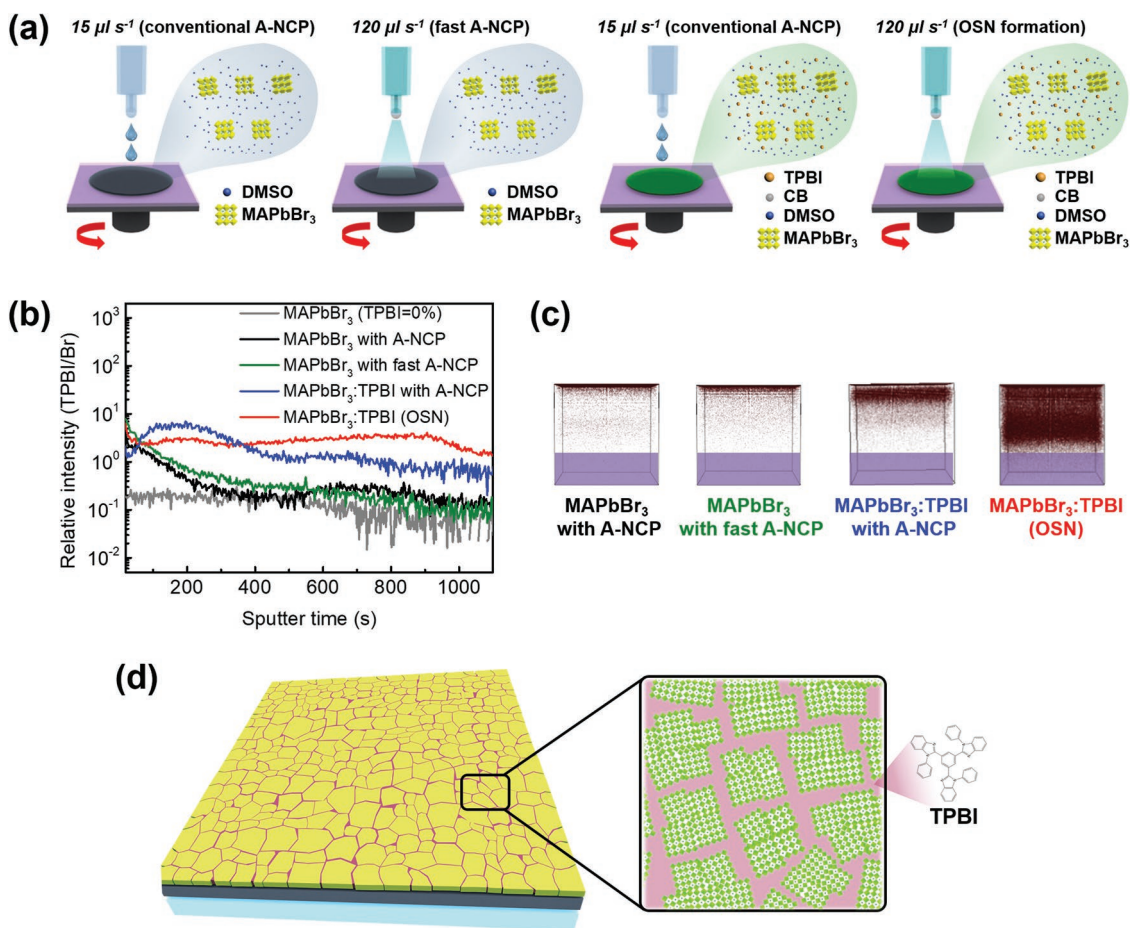


Figure 1. The fabrication of MAPbBr₃ films depending on the controlled A-NCP and precursor solutions. a) Illustrations of spin-coating processes investigated in the TOF-SIMS measurement depending on the controlled additive-based nanocrystal pinning (A-NCP) and precursor solutions with DMSO, MAPbBr₃, TPBI, and CB. b) Depth profiles of TPBI additive in the films measured by TOF-SIMS. c) Visualization images of TPBI distributions from TOF-SIMS results. d) Schematic illustration of TPBI-shielded MAPbBr₃ polycrystalline nanograins (OSN) mimicking core-shell nanoparticle.

the thermodynamically stable unsaturated to the unstable supersaturated states, and thus it can give the driving forces for nucleation to the unstable embryos and small crystals.^[33] We simply described the crystal growth mechanism by applying the LaMer model (Figure S7b, Supporting Information). In the fast A-NCP process for OSN film formation, the rapid co-evaporation of the solvents by volatile nonpolar CF induces 1) the simultaneous nucleation at most nucleation sites, 2) a short nucleation period, which induces uniform reactant reaction, to form small and uniform nanograins,^[34] 3) a short-time and instantaneous crystal growth that forms the small grains by the crystallographically misoriented faces related to grain boundaries,^[35] 4) a rapid consumption of limited precursor concentration, and 5) the instant rinsing of DMSO, the precursor diffusion medium. Therefore, fast A-NCP effectively causes the crystal growth to cease before secondary crystal growth by Ostwald ripening. On the other hand, when the spinning MAPbBr₃ quasi-film surface was slowly treated with a dripping speed of 15 μL s⁻¹ (A-NCP; Figure 1a),^[3,14] the solubility state of the spinning quasi-film could gradually change to the supersaturation state. A-NCP also gradually terminates the crystal growth before Ostwald ripening occurs. However, the TPBI molecules inside

the quasi-films are gradually rinsed away during A-NCP so that some portion of them cannot stay at grain boundaries and thus they do not have a uniform additive distribution throughout the film. On the other hand, fast A-NCP can effectively confine the additives in MAPbBr₃:TPBI quasi-film by instant DMSO rinsing for fast crystallization (Figure S7, Supporting Information).^[34,36]

To clarify the distribution of TPBI additives in the films, we used time-of-flight secondary ion mass spectroscopy (TOF-SIMS) (Figure 1b). A-NCP yielded similar profiles of TPBI additive distribution in pure MAPbBr₃ films regardless of dripping speed, but with very slight relative [TPBI] difference. On the other hand, the TPBI additive distribution in MAPbBr₃:TPBI films was greatly influenced by the crystal pinning processes (i.e., dripping speed of A-NCP). When MAPbBr₃:TPBI was treated by normal A-NCP, the rinsing by nonpolar CF caused a highly concentrated TPBI near the surface area than in the bulk. When the additives are unevenly distributed throughout the film: 1) the transports of charge carriers injected from electrodes can be unbalanced, so the electron-hole recombination cannot be efficient and the recombination zone can be locally formed close to the interface between EML and adjacent layers; 2) the unbalanced charge distribution causes the local charge

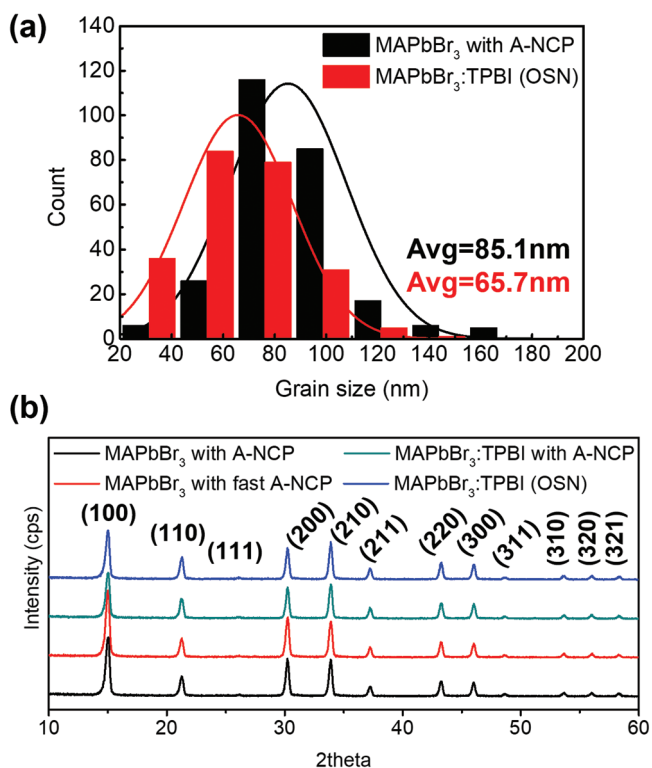


Figure 2. The grain size calculation and crystal structure analysis. a) Grain size distributions calculated from the SEM images depicted in Figure S11c,d in the Supporting Information. b) XRD patterns of MAPbBr₃ with controlled A-NCP, MAPbBr₃:TPBI with A-NCP, and MAPbBr₃:TPBI (OSN).

accumulation, which is accompanied by severe charge-exciton annihilation;^[37–39] 3) the local electric field can be generated by locally accumulated charges and migrated ions,^[40,41] so the material can be locally degraded and the device lifetime can be shortened by local Joule heating;^[37–39] and 4) uneven distribution of the organic semiconducting additives causes the uneven photo-physical properties of OIHPs.^[14,42] In contrast, MAPbBr₃:TPBI (OSN) film had uniform TPBI additive distribution from the top to the bottom throughout the film; this result means that the TPBI molecules are effectively captured in the film through the momentary crystallization by the drastic DMSO rinsing before the additives are washed. The uniform TPBI distribution

is advantageous because a charge localization can be avoided by effectively distributing the charge carriers and recombination region throughout the EML, and thus a radiative recombination rate can be improved. The visualized images easily confirm this conclusion (Figure 1c). We used SEM to observe the grain size and the surface morphologies of MAPbBr₃ with A-NCP and MAPbBr₃:TPBI (OSN) films (Figure S11, Supporting Information). MAPbBr₃:TPBI (OSN) film (average grain size = 65.7 nm; Figure 2a) had smaller grain size than did MAPbBr₃ film with A-NCP (average grain size = 85.1 nm; Figure 2a); this difference confirms that MAPbBr₃:TPBI (OSN) film effectively formed core-shell-mimicked nanograins, which is advantageous for the exciton confinement. All the controlled films showed the stable perovskite crystal structures with *Pm* $\bar{3}$ *m* cubic phase regardless of the types of precursor solution or the crystal-pinning process (Figure 2b). Therefore, we described the illustration of the core-shell nanoparticle-mimicked TPBI-shielded MAPbBr₃ nanograins as suggested (Figure 1d).

Steady-state and time-resolved PL characteristics were studied to investigate a radiative recombination behavior, PL dynamics, and the defect healing effect. MAPbBr₃:TPBI (OSN) film achieved a much higher steady-state PL intensity than MAPbBr₃ film with A-NCP (Figure 3a). The increased PL intensity was a consequence of the effective charge and exciton confinements inside the smaller nanograins and the increased effective area of passivated grain boundaries filled with TPBI additives.^[3,14] Moreover, the difference in PL intensities of MAPbBr₃:TPBI (OSN) film between the top surface and the bottom face was negligible although optical losses by SOCP and substrate interfaces were considered; this result is consistent with the uniform TPBI distribution throughout the film. In contrast, MAPbBr₃ film with A-NCP showed clear PL intensity difference between the top surface and the bottom face because TPBI additives were distributed preferentially close to the surface area (Figure 1b,c).^[14] Therefore, we conclude that the most grains in MAPbBr₃:TPBI (OSN) film can improve a radiative recombination by effectively confining the excitons, reduce the exciton dissociation at grain boundaries by defect healing effect, and distribute the charges in the film for higher electron-hole radiative recombination. We measured time-resolved PL to investigate the PL dynamics of the films. (Figure 3b and Table 1). The biexponential model was used to analyze the PL lifetime (τ) and the fraction (*f*) of each PL lifetime.

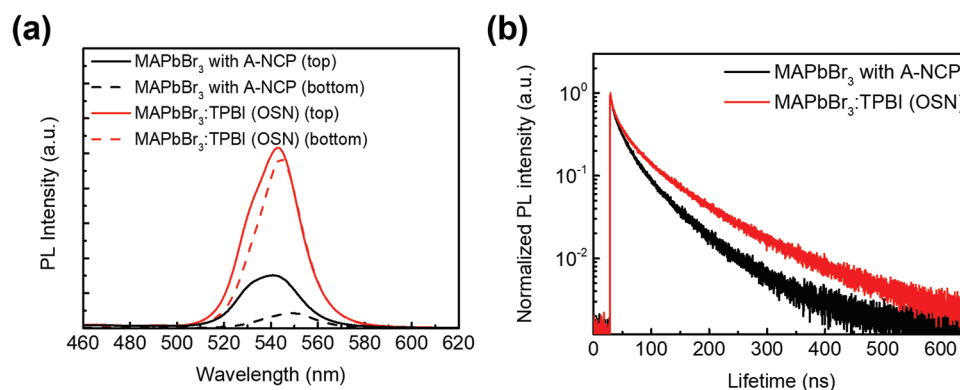


Figure 3. PL property measurements. a) Steady-state PL spectra and b) time-resolved PL of MAPbBr₃ with A-NCP and MAPbBr₃:TPBI (OSN) films.

Table 1. Summarized fast and slow PL lifetimes and fractions calculated by the biexponential decay model.

Films	τ_1 [ns]	f_1 [%]	τ_2 [ns]	f_2 [%]	τ_{avg} [ns]
MAPbBr ₃ with A-NCP	37.89	36.57	116.74	63.43	87.91
MAPbBr ₃ :TPBI (OSN)	46.99	34.34	131.96	65.66	102.78

The fast-decay components (τ_1 and f_1) are related to the trap-assisted nonradiative recombination at grain boundaries; the slow-decay components (τ_2 and f_2) are related to the radiative recombination inside the grains. MAPbBr₃:TPBI (OSN) film ($\tau_1 = 46.99$ ns, $\tau_2 = 131.96$ ns; $f_1 = 34.34\%$, $f_2 = 65.66\%$; $\tau_{\text{avg}} = 102.78$ ns) had higher τ_2 and f_2 than those of MAPbBr₃ film with A-NCP ($\tau_1 = 37.89$ ns, $\tau_2 = 116.74$ ns; $f_1 = 36.57\%$, $f_2 = 63.43\%$; $\tau_{\text{avg}} = 87.91$ ns); this increase means that 1) more effective exciton localization inside the core-shell-mimicked nanograins was achieved due to the smaller grain size,^[43] and 2) TPBI additives surrounding the nanograins more effectively healed the defect area in the grain boundary for more radiative recombination throughout the film,^[14] so radiative recombination rate in MAPbBr₃:TPBI (OSN) film was effectively increased. The trap-assisted nonradiative decay fraction (f_1) was reduced in MAPbBr₃:TPBI (OSN) film. Therefore, these positive effects throughout the film in OSN system are beneficial to the luminous efficiency in LEDs.^[43,44]

To confirm that the improved PL properties of uniform polycrystalline core-shell-mimicked nanograins affect the luminous efficiency in the devices, we fabricated PeLEDs that had simple structures of glass substrate/ SOCP (90 nm) as an anode and hole injection layer/EMLs (400 nm)/TPBI (50 nm) as an electron transporting layer (ETL)/LiF (1 nm) as an electron injection layer/Al (100 nm) as cathode. The OIHP EMLs were composed of MAPbBr₃ (A-NCP) or MAPbBr₃:TPBI (OSN) layers. The fabricated PeLEDs showed stable diode characteristics with very low leakage currents at low voltage (Figure S12, Supporting Information). The MAPbBr₃:TPBI (OSN) PeLED showed much higher EL efficiencies (EQE = 11.7% ph el⁻¹, CE = 45.95 cd A⁻¹) than MAPbBr₃ (A-NCP) PeLED (EQE = 8.64% ph el⁻¹, CE = 41.27 cd A⁻¹) (Figure 4a,b). Moreover, by using a half-sphere lens on top of the glass substrate of MAPbBr₃:TPBI (OSN) PeLED to further improve light out-coupling by reducing a substrate mode optical loss (Inset in Figure 4a; emissive pixels without and with a half-sphere lens), we achieved extremely high EL efficiencies of 21.81% ph el⁻¹ and 87.35 cd A⁻¹. The MAPbBr₃:TPBI (OSN) PeLED showed much lower operating current densities at the same luminance than the MAPbBr₃ (A-NCP) PeLED (Figure 4c); it occurs mainly because MAPbBr₃:TPBI (OSN) has more efficient radiative recombination with improved exciton confinement effect throughout the film. To ensure the measured EQE values, we measured angular emission intensity profiles. The angular emission intensity measurement was conducted after 150 s by applying a constant voltage of 5 V to be reliably measured with maintaining stable light emission intensity.^[13] The angular emission profiles of PeLEDs showed ideal Lambertian distributions (Figure 4d). It is surely advantageous to the application of LEDs.

Capacitance–voltage measurement has been used to define the charge accumulation behavior in electronic devices. The

MAPbBr₃:TPBI (OSN) PeLED showed the decreased maximum capacitance. This can be ascribed to decrease of ion migration due to the TPBI shell surrounding the MAPbBr₃ nanograins in the OSN film (Figure 4e).^[45] Moreover, the device half-lifetime of MAPbBr₃:TPBI (OSN) PeLED was highly improved more than four-times than MAPbBr₃ (A-NCP) PeLED ($t_{50} = 251$ min for MAPbBr₃:TPBI (OSN), 58.2 min for MAPbBr₃ (A-NCP)) because of more uniform electron–hole recombination and reduced ion migration throughout the film with uniform TPBI distribution (Figure 4f).

In order to improve light extraction efficiency in conventional LEDs, the effective way is to reduce an internal optical loss such as a waveguide mode. The higher optical constant values of OIHPs than those of organic films have been reported.^[46,47] The big difference in the refractive indices ($n = 2.4$ – 2.6 for CH₃NH₃PbI_{3-x}Cl_x and 1.4 – 2.3 for organic thin film in the visible range) causes a high optical loss by the internal light reflection at the interface between OIHP and organic layers, and the reflected light can be reabsorbed into the OIHPs due to the high extinction coefficient (k) of OIHPs.^[46,47] The optical constants of pristine OIHPs can be one of the constraints on the out-coupling efficiency in PeLEDs. Core-shell-mimicked polycrystalline OIHP:additive film can be a solution to achieve higher out-coupling due to much lower n than that of pristine OIHPs. To further understand the improvement in terms of optical effects in MAPbBr₃:TPBI (OSN), we performed spectroscopic ellipsometry using a general oscillator (GenOsc) model to determine the optical constants (n and k) of pure MAPbBr₃ (without TPBI additive) and MAPbBr₃:TPBI (OSN) films.^[48] We used measured n and k for the optical simulations to determine the additional origin of high EQE in MAPbBr₃:TPBI (OSN) PeLEDs. The n and k of MAPbBr₃:TPBI (OSN) clearly differed from those of pure MAPbBr₃ (Figure 5a,b). It means that the reduced n of MAPbBr₃:TPBI (OSN) EML ($n = 1.7$ at 540 nm) approached that of a polymeric anode (SOCP, $n = 1.43$ at 540 nm),^[49] and thus the small difference in n increases light extraction efficiency by reducing the internal light reflection by the waveguide mode at the SOCP–EML interface although other optical losses can be increased by increase in k of MAPbBr₃:TPBI (OSN).^[50] To identify the origin of the changes in optical parameters by the different crystallization, we also fabricated pure MAPbBr₃ films by controlling dropping speed using pure CF solvent without TPBI additive (CF with 15 $\mu\text{L s}^{-1}$, CF-15; CF with 120 $\mu\text{L s}^{-1}$, CF-120). We confirmed that the optical properties of pure MAPbBr₃ film were definitely dependent on the speed of the dropping process (Figure S13, Supporting Information). In MAPbBr₃ with CF-120, absorbance A increased by 38%, and transmittance T decreased by 82% at 540 nm (Figure S13a,b, Supporting Information). The difference in the values of n and k supported the difference in A and T by the dropping speed (Figure S13c, Supporting Information). In MAPbBr₃ with CF-120, n decreased

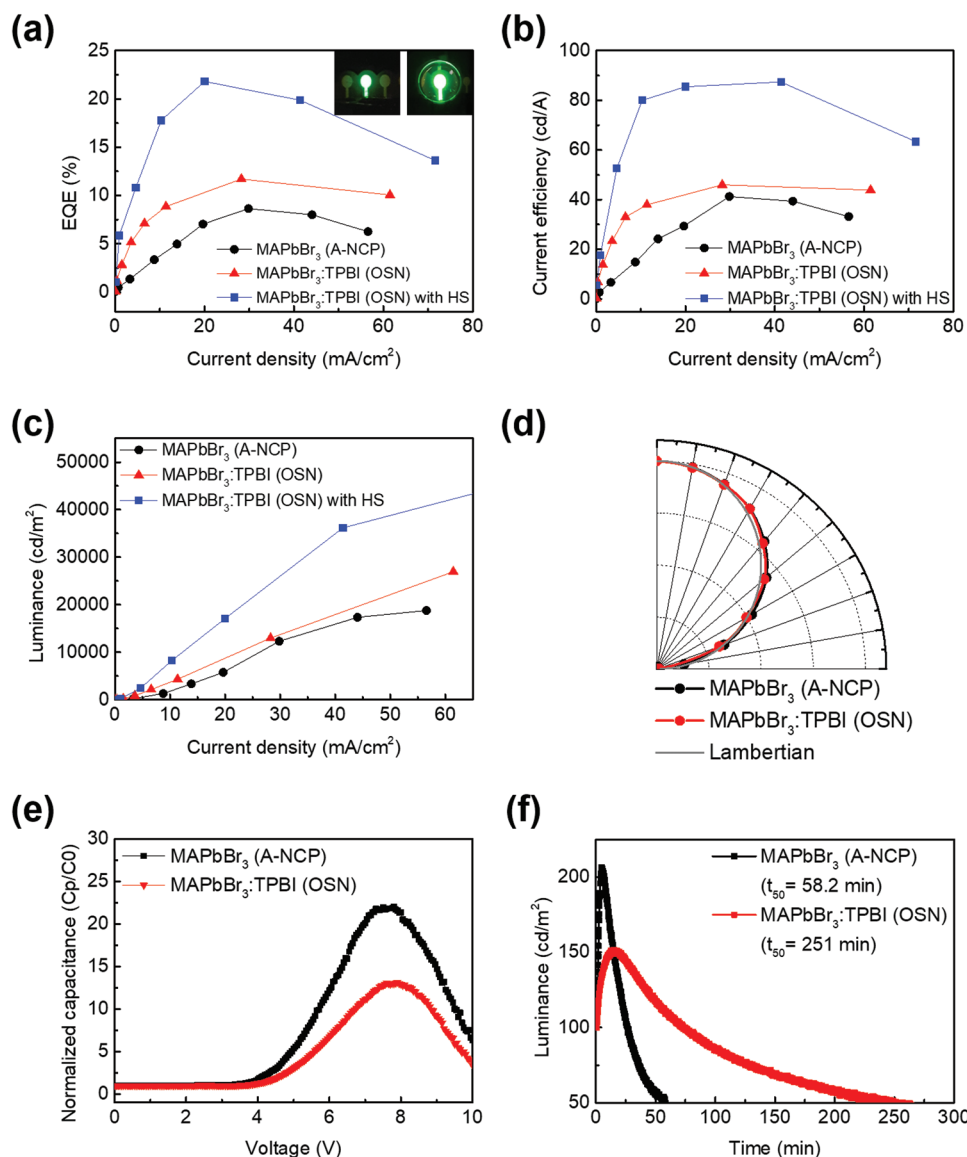


Figure 4. Device characteristics of PeLEDs based on MAPbBr₃ (A-NCP) and MAPbBr₃:TPBI (OSN) EMLs and OSN PeLED with half-sphere lens (HS). a) EQE versus current density (inset: emitting pixels without and with HS). b) Current efficiency versus current density. c) Luminance versus current density. d) Angle-dependent EL intensities. e) Capacitance versus voltage measurement. f) Half-lifetime measurement with constant current corresponding to the luminance of 100 cd m⁻².

and k increased at 540 nm; both changes were similar to the case of MAPbBr₃:TPBI (OSN) (Figure 5a,b). The difference is also obvious to the naked eye (Figure S13d; left: MAPbBr₃ with CF-15, right: MAPbBr₃ with CF-120, Supporting Information). High dropping speed (i.e., inducing rapid solubility change of quasi-film) can provide higher porosity with the randomly oriented grain growth, and thereby a higher free volume between grains can affect the optical parameters of the OIHP film (Figure S14, Supporting Information). Therefore, we can conclude that the higher porosity will be the main factor that changed the optical properties (n , k , A , and T) of MAPbBr₃:TPBI (OSN) film. In contour plots of simulated relative out-coupled power ratio from OIHP (η_{OIHP}) as a function of EML thickness and emitter position (Figure 5c,d),

pure MAPbBr₃ showed relatively lower η_{OIHP} at all emitter positions than did MAPbBr₃:TPBI (OSN). Moreover, η_{OIHP} of MAPbBr₃:TPBI (OSN) was highest when the emitter was positioned around the EML-SOCP interface; relative η_{OIHP} did not increase much when the emitter was placed near the ETL-EML interface due to strong self-absorption property of OIHPs. When the recombination zone is shifted toward the anode, the optical out-coupling is more beneficial. The shift of recombination zone toward EML-SOCP interface was confirmed by redshifted EL spectrum of MAPbBr₃:TPBI (OSN) PeLED compared to the EL spectrum of MAPbBr₃ (A-NCP) PeLED (Figure S15, Supporting Information). Therefore, the optical simulation results explained higher EQE by reducing the loss of waveguide mode.

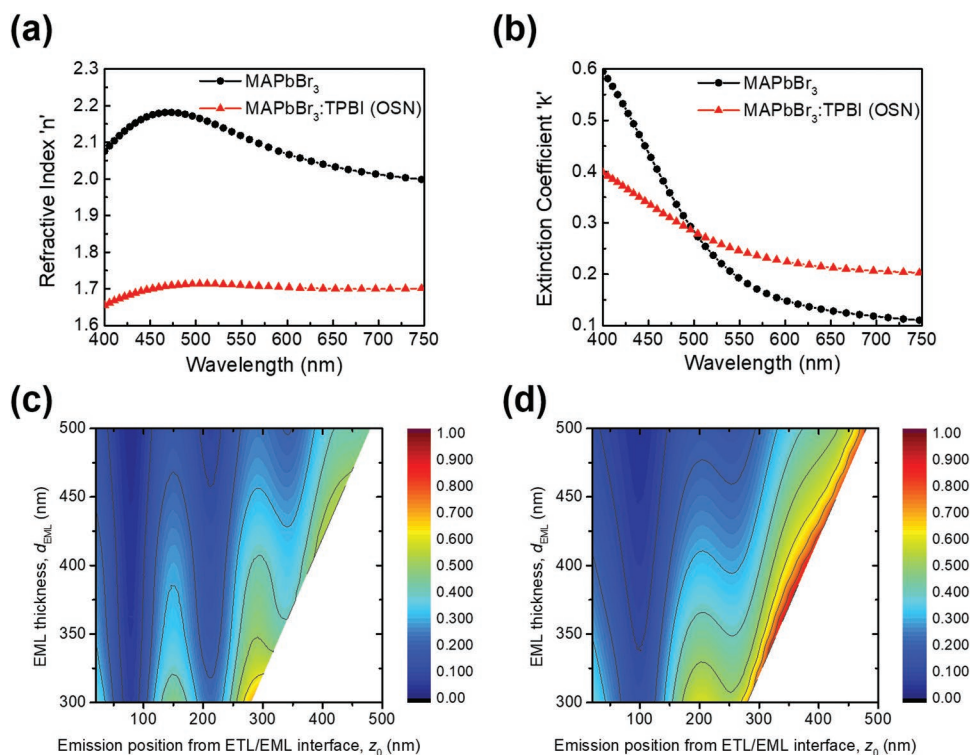


Figure 5. Spectroscopic ellipsometry measurement using the GenOsc model and optical simulation results of pure MAPbBr₃ and MAPbBr₃:TPBI (OSN). a) Refractive index. b) Extinction coefficient. c,d) Optical simulations of relative out-coupled power ratio (η_{OIHP}) for PeLEDs based on c) pure MAPbBr₃ and d) MAPbBr₃:TPBI (OSN).

3. Conclusion

In summary, we developed polycrystalline core-shell-mimicked nanograins consisting of core MAPbBr₃ nanograins shielded with semiconducting TPBI additives to mimic core-shell nanoparticles. We investigated the influence of the organic small molecule additive on OIHP crystallization kinetics when the conventional spin-coating process was used for additive-mixed OIHP film formation, and observed that TPBI additive severely affected the crystal growth behavior by Ostwald ripening that is unfavorable for the efficient LED application. Therefore, we devised a new polycrystal system, core-shell-mimicked OSN, by controlling the crystallization kinetics of MAPbBr₃:TPBI quasi-film and form small nanograins (i.e., core) shielded with a uniform TPBI additive that uniformly filled the whole defective grain boundary region throughout the film to provide efficient defect passivation; as a result, charge carriers and excitons are more effectively confined spatially inside nanograins instead of being dissociated to free charge carriers to give a higher radiative recombination rate uniformly throughout the film. The MAPbBr₃:TPBI (OSN) also facilitated effective light out-coupling due to the low optical loss at the SOCP-EML interface. As a result, the MAPbBr₃:TPBI (OSN) PeLED achieved high device efficiencies (EQE = 21.81% ph el⁻¹; CE = 87.35 cd A⁻¹ with a half-sphere lens). Moreover, the half-lifetime was increased by more than four times. Therefore, our approach will give the insights into guide the future study in PeLEDs using 3D polycrystalline OIHPs to overcome their limitation of EL efficiency and lifetime.

4. Experimental Section

Sample Preparation: SOCP was prepared by using poly(3,4-ethylenedioxythiophene):poly(styrenesulfonate):perfluorinated ionomer (PEDOT:PSS (Clevios PH500):PFI = 1:2.5:11.2 (w:w:w)) solution with 5 wt% DMSO additive. About 40 wt% MAPbBr₃:DMSO solution was synthesized by using MABr and PbBr₂ in a 1.06:1 molar ratio. After the TPBI:CB and MAPbBr₃ solutions were synthesized, uniform organic small molecule additive-mixed OIHP materials were obtained by directly mixing TPBI solution in a ratio of 1:5 (vol:vol) with MAPbBr₃ solution.

PeLED Fabrication: SOCP on a glass substrate was used as a functional polymeric anode that also functioned as a hole injection layer. A layer of SOCP (90 nm) was spin-coated, then baked at 200 °C for 10 min. MAPbBr₃ (A-NCP) and MAPbBr₃:TPBI (OSN) films as EMLs were spin-coated in a N₂-filled glove box and then annealed at 90 °C for 10 min, then loaded into an ultrahigh vacuum chamber ($\approx 10^{-7}$ Torr) to thermally deposit 50 nm thick TPBI as an electron transport layer, 1 nm thick LiF as an electron injection layer, and 100 nm thick Al as a cathode. Fabricated PeLEDs were encapsulated by using a hollow glass and UV-curable epoxy resin.

Film Characterization: MAPbBr₃ surface was measured using a high-resolution field-emission SEM with dual EDS (JSM-7800F Prime). The crystal structure was defined using XRD (Rigaku, D/MAX-2500). To define additive distribution in the films, TOF-SIMS (ION-TOF GmbH, Münster, Germany) measurement was conducted at the KBSI Busan Center by using a pulsed 30 keV Bi⁺ primary beam with a current of 0.64 pA. The analyzed area used in this work was a square of 200 μm \times 200 μm . A negative ion spectra were internally calibrated using H⁻, C⁻, C₂⁻, C₃⁻, and C₄⁻ peaks, and a positive ion spectra were internally calibrated using H⁺, CH₃⁺, C₂H₅⁺, C₃H₇⁺, and C₄H₉⁺ normalized to the respective secondary total ion yields. The depth profile was a square of 500 μm \times 500 μm using a 5 keV Ar cluster. Steady-state PL was measured by using a JASCO FP6500 spectrofluorometer with an excitation wavelength of 405 nm. Time-correlated single photon

counting (TCSPC) was conducted using a PicoHarp 300 TCSPC module (PicoQuant GmbH), which includes a picosecond pulsed laser head (LDH-P-C-405B, PicoQuant, 405 nm excitation wavelength, ≈ 150 fs pulse width) driven by a PLD800-D laser driver at 40 MHz repetition rate as excitation source equipped with a monochromator (SP-2155, Acton) and MCP-PMT (R3809U-50, Hamamatsu). Optical constants (n and k) of MAPbBr₃ and MAPbBr₃:TPBI were measured by using variable angle spectroscopic ellipsometry (VASE, J.A. Woollam Inc.) between 0.7 and 6 eV at incidence angles of 65°, 70°, and 75°. Absorbance and transmittance of MAPbBr₃ films were measured using a UV spectrometer (S3100, Scinco).

PeLED Characterization: Current density–voltage–luminance characteristics were measured using a power source (Keithley 236) and an EL spectroradiometer (Minolta CS-2000). Capacitance–voltage characterizations were conducted using electrochemical impedance spectroscopy (Bio-Logic SP-300). All PeLEDs were biased from 0 to 10 V with a constant frequency of 1000 Hz in darkness. The angular-dependent EL characteristics were measured using a custom automated goniometric system which consists of a fiber-optic spectrometer (EPP2000, Stellarnet, Inc.) and a calibrated photodiode (FDS-100-CAL, Thorlabs, Inc.) connected with HP4140B (Hewlett Packard). All the measurements were performed under ambient N₂ after device encapsulation. Half-lifetimes were measured by recording the luminance change at constant current that corresponds to a luminance of 100 cd m⁻² (M6000, Polaronix). The half-sphere lens (radius: 5 mm, thickness: 5 mm, Edmund Optics Inc., USA) and an index matching fluid (F-IMS-105, $n = 1.52$ at 589 nm; viscosity = 100 cps, Newport Co., USA) were used to improve light out-coupling of PeLEDs. To measure the light output of PeLED with a half-sphere lens, a 6 in. integrating sphere (IS-6, Stellarnet, Tampa, USA) and a BLUE-Wave spectrometer (BW-VIS, Stellarnet) were used.

FTIR Measurement: FTIR (Nicolet iS10 FTIR spectrometer, Thermo Fisher Scientific) transmittance spectra were measured in real time depending on the drying time. Equimolar amounts of MABr, PbBr₂, DMSO, and TPBI additive were dissolved in the DMF to synthesize 0.03 M solutions. Each drop of the synthesized solutions was dried in the air-flow condition and the transmittance spectra were measured in the stable air condition in real time.

Optical Simulation: The optical model used for the device analysis is based on the classical dipole approximation of the source geometry.^[51,52] To incorporate the nontrivial absorption in the OIHP layer, the generalized formulation on absorbing cavity was adopted.^[53] For the generalized transmittance, the transfer matrix formalism summarized by Centurioni was used.^[54] A custom MATLAB code was used for the actual simulation. For simplicity, internal quantum efficiency (IQE) was assumed to be unity. The refractive indices of Al, TPBI, SOCP, and glass used for the optical simulation were measured using spectroscopic ellipsometry (Woollam M2000D).

Another optical model used to analyze emission spectrum shift is based on the two-beam interference equation in the planar Fabry–Pérot cavity considering normal directional emission (Equation (1); Figure S15b–d, Supporting Information).^[55] Transfer matrix formalism was used to calculate effective reflectance from the cathode.

$$f_{\text{TI}} = 1 + R_{\text{cathode}} + 2\sqrt{R_{\text{cathode}}} \cos\left(-\phi_{\text{cathode}} + \frac{4\pi}{\lambda_{\text{OIHP}}} z_0\right) \quad (1)$$

The PL spectrum measured from bottom direction was used to analyze peak emission spectrum. Overall spectrum was calculated by multiplying two-beam interference equation and PL spectrum. Peak emission spectrum was extracted from the calculated spectrum (Equation (2)).

$$\lambda_{\text{peak}}(z_0) = \arg \max(f_{\text{TI}}(\lambda) \times S_{\text{PL, top}}(\lambda)) \quad (2)$$

Peak emission spectrum shift was obtained by subtracting calculated spectrum from the original PL spectrum (Equation (3)).

$$\Delta\lambda_{\text{peak}} = \lambda_{\text{peak}}(z_0) - \lambda_{0\text{peak}} \quad (3)$$

Supporting Information

Supporting Information is available from the Wiley Online Library or from the author.

Acknowledgements

This work was supported by the National Research Foundation of Korea (NRF) grant funded by the Korea government (Ministry of Science, ICT & Future Planning) (NRF-2016R1A3B1908431).

Conflict of Interest

The authors declare no conflict of interest.

Keywords

external quantum efficiency, nanograin, organic–inorganic halide perovskite polycrystal, out-coupling, perovskite light-emitting diode

Received: March 8, 2019
Published online: April 2, 2019

- [1] Z.-K. Tan, R. S. Moghaddam, M. L. Lai, P. Docampo, R. Higler, F. Deschler, M. Price, A. Sadhanala, L. M. Pazos, D. Credgington, F. Hanusch, T. Bein, H. J. Snaith, R. H. Friend, *Nat. Nanotechnol.* **2014**, *9*, 687.
- [2] Y.-H. Kim, H. Cho, J. H. Heo, T.-S. Kim, N. Myoung, C.-L. Lee, S. H. Im, T.-W. Lee, *Adv. Mater.* **2015**, *27*, 1248.
- [3] H. Cho, S.-H. Jeong, M.-H. Park, Y.-H. Kim, C. Wolf, C.-L. Lee, J. H. Heo, A. Sadhanala, N. Myoung, S. Yoo, S. H. Im, R. H. Friend, T.-W. Lee, *Science* **2015**, *350*, 1222.
- [4] Y.-H. Kim, H. Cho, T.-W. Lee, *Proc. Natl. Acad. Sci. USA* **2016**, *113*, 11694.
- [5] J. Byun, H. Cho, C. Wolf, M. Jang, A. Sadhanala, R. H. Friend, H. Yang, T.-W. Lee, *Adv. Mater.* **2016**, *28*, 7515.
- [6] M. Yuan, L. N. Quan, R. Comin, G. Walters, R. Sabatini, O. Voznyy, S. Hoogland, Y. Zhao, E. M. Beauregard, P. Kanjanaboos, Z. Lu, D. H. Kim, E. H. Sargent, *Nat. Nanotechnol.* **2016**, *11*, 872.
- [7] L. Zhang, X. Yang, Q. Jiang, P. Wang, Z. Yin, X. Zhang, H. Tan, Y. M. Yang, M. Wei, B. R. Sutherland, E. H. Sargent, J. You, *Nat. Commun.* **2017**, *8*, 15640.
- [8] J. Song, J. Li, X. Li, L. Xu, Y. Dong, H. Zeng, *Adv. Mater.* **2015**, *27*, 7162.
- [9] J. Wang, N. Wang, Y. Jin, J. Si, Z.-K. Tan, H. Du, L. Cheng, X. Dai, S. Bai, H. He, Z. Ye, M. L. Lai, R. H. Friend, W. Huang, *Adv. Mater.* **2015**, *27*, 2311.
- [10] H. Zhou, Q. Chen, G. Li, S. Luo, T.-b. Song, H.-S. Duan, Z. Hong, J. You, Y. Liu, Y. Yang, *Science* **2014**, *345*, 542.
- [11] H. Do Kim, H. Ohkita, H. Benten, S. Ito, *Adv. Mater.* **2016**, *28*, 917.
- [12] H. Hu, T. Salim, B. Chen, Y. M. Lam, *Sci. Rep.* **2016**, *6*, 33546.
- [13] Z. Xiao, R. A. Kerner, L. Zhao, N. L. Tran, K. M. Lee, T.-W. Koh, G. D. Scholes, B. P. Rand, *Nat. Photonics* **2017**, *11*, 108.
- [14] M.-H. Park, S.-H. Jeong, H.-K. Seo, C. Wolf, Y.-H. Kim, H. Kim, J. Byun, J. S. Kim, H. Cho, T.-W. Lee, *Nano Energy* **2017**, *42*, 157.
- [15] K. Lin, J. Xing, L. N. Quan, F. P. G. de Arquer, X. Gong, J. Lu, L. Xie, W. Zhao, D. Zhang, C. Yan, W. Li, X. Liu, Y. Lu, J. Kirman, E. H. Sargent, Q. Xiong, Z. Wei, *Nature* **2018**, *562*, 245.
- [16] Y. Cao, N. Wang, H. Tian, J. Guo, Y. Wei, H. Chen, Y. Miao, W. Zou, K. Pan, Y. He, H. Cao, Y. Ke, M. Xu, Y. Wang, M. Yang, K. Du, Z. Fu,

- D. Kong, D. Dai, Y. Jin, G. Li, H. Li, Q. Peng, J. Wang, W. Huang, *Nature* **2018**, 562, 249.
- [17] B. Zhao, S. Bai, V. Kim, R. Lamboll, R. Shivanna, F. Auras, J. M. Richter, L. Yang, L. Dai, M. Alsari, X.-J. She, L. Liang, J. Zhang, S. Lilliu, P. Gao, H. J. Snaith, J. Wang, N. C. Greenham, R. H. Friend, D. Di, *Nat. Photonics* **2018**, 12, 783.
- [18] V. D'Innocenzo, G. Grancini, M. J. P. Alcocer, A. R. S. Kandada, S. D. Stranks, M. M. Lee, G. Lanzani, H. J. Snaith, A. Petrozza, *Nat. Commun.* **2014**, 5, 3586.
- [19] Y.-H. Kim, C. Wolf, Y.-T. Kim, H. Cho, W. Kwon, S. Do, A. Sadhanala, C. G. Park, S.-W. Rhee, S. H. Im, R. H. Friend, T.-W. Lee, *ACS Nano* **2017**, 11, 6586.
- [20] T. Chiba, Y. Hayashi, H. Ebe, K. Hoshi, J. Sato, S. Sato, Y.-J. Pu, S. Ohisa, J. Kido, *Nat. Photonics* **2018**, 12, 681.
- [21] D. W. de Quilettes, S. M. Vorpahl, S. D. Stranks, H. Nagaoka, G. E. Eperon, M. E. Ziffer, H. J. Snaith, D. S. Ginger, *Science* **2015**, 348, 683.
- [22] C.-Y. Chang, C.-Y. Chu, Y.-C. Huang, C.-W. Huang, S.-Y. Chang, C.-A. Chen, C.-Y. Chao, W.-F. Su, *ACS Appl. Mater. Interfaces* **2015**, 7, 4955.
- [23] M. K. Kim, T. Jeon, H. Il Park, J. M. Lee, S. A. Nam, S. O. Kim, *Cryst. EngComm* **2016**, 18, 6090.
- [24] M. Rauls, K. Bartosch, M. Kind, S. Kuch, R. Lacmann, A. Mersmann, *J. Cryst. Growth* **2000**, 213, 116.
- [25] M. Becker, M. Wark, *Org. Electron.* **2017**, 50, 87.
- [26] T.-W. Koh, J.-M. Choi, S. Lee, S. Yoo, *Adv. Mater.* **2010**, 22, 1849.
- [27] Y. Du, H. Cai, H. Wen, Y. Wu, Z. Li, J. Xu, L. Huang, J. Ni, J. Li, J. Zhang, *RSC Adv.* **2016**, 6, 83264.
- [28] N. Kubota, M. Yokota, J. Mullin, *J. Cryst. Growth* **2000**, 212, 480.
- [29] J. Xu, A. Buin, A. H. Ip, W. Li, O. Voznyy, R. Comin, M. Yuan, S. Jeon, Z. Ning, J. J. McDowell, P. Kanjanaboos, J.-P. Sun, X. Lan, L. N. Quan, D. H. Kim, I. G. Hill, P. Maksymovych, E. H. Sargent, *Nat. Commun.* **2015**, 6, 7081.
- [30] M. Hadadian, J.-P. Correa-Baena, E. K. Goharshadi, A. Ummadisingu, J.-Y. Seo, J. Luo, S. Gholipour, S. M. Zakeeruddin, M. Saliba, A. Abate, M. Grätzel, A. Hagfeldt, *Adv. Mater.* **2016**, 28, 8681.
- [31] C.-H. Chiang, C.-G. Wu, *Nat. Photonics* **2016**, 10, 196.
- [32] C. Qin, T. Matsushima, T. Fujihara, C. Adachi, *Adv. Mater.* **2017**, 29, 1603808.
- [33] D. Liu, W. Zhou, H. Tang, P. Fu, Z. Ning, *Sci. China: Chem.* **2018**, 61, 1278.
- [34] S. Engberg, Z. Li, J. Y. Lek, Y. M. Lam, J. Schou, *RSC Adv.* **2015**, 5, 96593.
- [35] B. Roose, A. Ummadisingu, J.-P. Correa-Baena, M. Saliba, A. Hagfeldt, M. Graetzel, U. Steiner, A. Abate, *Nano Energy* **2017**, 39, 24.
- [36] M. Keating, Y. Chen, I. A. Larmour, K. Faulds, D. Graham, *Meas. Sci. Technol.* **2012**, 23, 084006.
- [37] A. L. Palma, L. Cina, Y. Busby, A. Marsella, A. Agresti, S. Pescetelli, J. J. Pireaux, A. Di Carlo, *ACS Appl. Mater. Interfaces* **2016**, 8, 26989.
- [38] X. Li, X.-A. Cao, *Org. Electron.* **2013**, 14, 2523.
- [39] P. Cusumano, *Synth. Met.* **2003**, 139, 657.
- [40] W. Tress, N. Marinova, T. Moehl, S. M. Zakeeruddin, M. K. Nazeeruddin, M. Grätzel, *Energy Environ. Sci.* **2015**, 8, 995.
- [41] J. M. Azpiroz, E. Mosconi, J. Bisquert, F. De Angelis, *Energy Environ. Sci.* **2015**, 8, 2118.
- [42] Y. Shao, Z. Xiao, C. Bi, Y. Yuan, J. Huang, *Nat. Commun.* **2014**, 5, 5784.
- [43] H. He, Q. Yu, H. Li, J. Li, J. Si, Y. Jin, N. Wang, J. Wang, J. He, X. Wang, Y. Zhang, Z. Ye, *Nat. Commun.* **2016**, 7, 10896.
- [44] S. F. Chichibu, T. Onuma, T. Aoyama, K. Nakajima, P. Ahmet, T. Chikow, T. Sota, S. P. DenBaars, S. Nakamura, T. Kitamura, Y. Ishida, H. Okumura, *J. Vac. Sci. Technol., B: Microelectron. Process. Phenom* **2003**, 21, 1856.
- [45] Y.-H. Kim, G.-H. Lee, Y.-T. Kim, C. Wolf, H. J. Yun, W. Kwon, C. G. Park, T.-W. Lee, *Nano Energy* **2017**, 38, 51.
- [46] C.-W. Chen, S.-Y. Hsiao, C.-Y. Chen, H.-W. Kang, Z.-Y. Huang, H.-W. Lin, *J. Mater. Chem. A* **2015**, 3, 9152.
- [47] D. Yokoyama, *J. Mater. Chem.* **2011**, 21, 19187.
- [48] M. S. Alias, I. Dursun, M. I. Saidaminov, E. M. Diallo, P. Mishra, T. K. Ng, O. M. Bakr, B. S. Ooi, *Opt. Express* **2016**, 24, 16586.
- [49] S.-H. Jeong, S.-H. Woo, T.-H. Han, M.-H. Park, H. Cho, Y.-H. Kim, H. Cho, H. Kim, S. Yoo, T.-W. Lee, *NPG Asia Mater.* **2017**, 9, e411.
- [50] J. Lee, T.-H. Han, M.-H. Park, D. Y. Jung, J. Seo, H.-K. Seo, H. Cho, E. Kim, J. Chung, S.-Y. Choi, T.-S. Kim, T.-W. Lee, S. Yoo, *Nat. Commun.* **2016**, 7, 11791.
- [51] M. Furno, R. Meerheim, S. Hofmann, B. Lüssem, K. Leo, *Phys. Rev. B* **2012**, 85, 115205.
- [52] K. A. Neyts, *J. Opt. Soc. Am. A* **1998**, 15, 962.
- [53] M. S. Tomaš, Z. Lenac, *Phys. Rev. A* **1997**, 56, 4197.
- [54] E. Centurioni, *Appl. Opt.* **2005**, 44, 7532.
- [55] H. Cho, C. Yun, S. Yoo, *Opt. Express* **2010**, 18, 3404.